CHANGES IN THE PHYSICAL ENVIRONMENT OF THE INNER COMA OF 67P/CHURYUMOV–GERASIMENKO WITH DECREASING HELIOCENTRIC DISTANCE

D. Bodewits[1], L. M. Lara[2], M. F. A'Hearn[1,3], F. La Forgia[4], A. Gicquel[5], G. Kovacs[5], J. Knollenberg[6], M. Lazzarin[4], Z.-Y. Lin (林忠義)[7], X. Shi[5], C. Snodgrass[8], C. Tubiana[5], H. Sierks[5], C. Barbieri[4], P. L. Lamy[9], R. Rodrigo[10,11], D. Koschny[12], H. Rickman[13], H. U. Keller[14], M. A. Barucci[15], J.-L. Bertaux[16], I. Bertini[17], S. Boudreault[5], G. Cremonese[18], V. Da Deppo[19], B. Davidsson[13], S. Debei[20], M. De Cecco[21], S. Fornasier[15], M. Fulle[22], O. Groussin[9], P. J. Gutiérrez[2], C. Güttler[5], S. F. Hviid[6], W.-H. Ip[23], L. Jorda[9], J.-R. Kramm[5], E. Kührt[6], M. Küppers[24], J. J. López-Moreno[2], F. Marzari[4], G. Naletto[4,19,25], N. Oklay[5], N. Thomas[26,27], I. Toth[28], and J.-B. Vincent[5]

[1] Department of Astronomy, University of Maryland, College Park, MD 20742-2421, USA; Dennis@astro.umd.edu
[2] Instituto de Astrofisica de Andalucia–CSIC, Glorieta de la Astronomia, E-18008 Granada, Spain
[3] Gauss Professor, Akademie der Wissenschaften zu Göttingen, D-37077 Göttingen, Germany
[4] University of Padova, Department of Physics and Astronomy, Vicolo dell'Osservatorio 3, I-35122 Padova, Italy
[5] Max-Planck Institut für Sonnensystemforschung, Justus-von-Liebig-Weg, 3 D-37077 Göttingen, Germany
[6] Deutsches Zentrum für Luft- und Raumfahrt (DLR), Institut für Planetenforschung, Rutherfordstrasse 2, D-12489 Berlin, Germany
[7] Institute of Astronomy, National Central University, Chung-Li 32054, Taiwan
[8] Planetary and Space Sciences, Department of Physical Sciences, The Open University, Milton Keynes MK7 6AA, UK
[9] Aix Marseille Université, CNRS, LAM (Laboratoire d'Astrophysique de Marseille), UMR 7326, F-13388 Marseille, France
[10] Centro de Astrobiología, CSIC-INTA, E-28850 Torrejón de Ardoz, Madrid, Spain
[11] International Space Science Institute, Hallerstraße 6, 3012 Bern, Switzerland
[12] Scientific Support Office, European Space Research and Technology Centre/ESA, Keplerlaan 1, Postbus 299, 2201 AZ Noordwijk ZH, The Netherlands
[13] Department of Physics and Astronomy, Uppsala University, Box 516, SE-75120 Uppsala, Sweden
[14] Institut für Geophysik und extraterrestrische Physik (IGEP), Technische Universität Braunschweig, Mendelssohnstr. 3, D-38106 Braunschweig, Germany
[15] LESIA–Observatoire de Paris, CNRS, Université Pierre et Marie Curie, Université Paris Diderot, 5, Place J. Janssen, F-92195 Meudon Principal Cedex, France
[16] LATMOS, CNRS/UVSQ/IPSL, 11 Boulevard d'Alembert, F-78280 Guyancourt, France
[17] Centro di Ateneo di Studi ed Attivitá Spaziali "Giuseppe Colombo" (CISAS), University of Padova, Via Venezia 15, I-35131 Padova, Italy
[18] INAF, Osservatorio Astronomico di Padova, Vicolo dell'Osservatorio 5, I-35122 Padova, Italy
[19] CNR-IFN UOS Padova LUXOR, Via Trasea, 7, I-35131 Padova, Italy
[20] Department of Industrial Engineering, University of Padova, Via Venezia, 1, I-35131 Padova, Italy
[21] University of Trento, via Sommarive, 9, I-38123 Trento, Italy
[22] INAF—Osservatorio Astronomico di Trieste, Via Tiepolo 11, I-34014 Trieste, Italy
[23] Institute for Space Science, National Central University, 32054 Chung-Li, Taiwan
[24] Operations Department, European Space Astronomy Centre/ESA, P.O. Box 78, E-28691 Villanueva de la Cañada (Madrid), Spain
[25] Department of Information Engineering, University of Padova, Via Gradenigo 6/B, I-35131 Padova, Italy
[26] Physikalisches Institut der Universität Bern, Sidlerstr. 5, 3012 Bern, Switzerland
[27] Center for Space and Habitability, University of Bern, 3012 Bern, Switzerland
[28] MTA CSFK Konkoly Observatory, Konkoly Thege M. ut 15/17, HU 1525 Budapest, Hungary

ABSTRACT

The Wide Angle Camera of the OSIRIS instrument on board the *Rosetta* spacecraft is equipped with several narrow-band filters that are centered on the emission lines and bands of various fragment species. These are used to determine the evolution of the production and spatial distribution of the gas in the inner coma of comet 67P with time and heliocentric distance, here between 2.6 and 1.3 au pre-perihelion. Our observations indicate that the emission observed in the OH, O I, CN, NH, and NH_2 filters is mostly produced by dissociative electron impact excitation of different parent species. We conclude that CO_2 rather than H_2O is a significant source of the [O I] 630 nm emission. A strong plume-like feature observed in the CN and O I filters is present throughout our observations. This plume is not present in OH emission and indicates a local enhancement of the CO_2/H_2O ratio by as much as a factor of 3. We observed a sudden decrease in intensity levels after 2015 March, which we attribute to decreased electron temperatures in the first few kilometers above the surface of the nucleus.

Key words: atomic processes – comets: individual (67P/Churyumov–Gerasimenko) – molecular processes – plasmas – radiation mechanisms: non-thermal – techniques: image processing

1. INTRODUCTION

Comets are considered to be relatively pristine leftovers from the early days of our solar system. They are distinguished from other minor bodies by a coma of gas and dust produced when ices retained from the formation of the solar system sublime. Understanding the connection between the coma and the comet's nucleus is critical because observations rarely detect the nucleus directly, and its properties must often be inferred from measurements of the surrounding coma. Because measurements of the coma do not necessarily represent the characteristics of the nucleus due to spatial, temporal and chemical evolution of the emitted material, projecting the coma observations back to the nucleus requires an understanding of the processes that induce changes in the coma. Compositional

Table 1
Observing Log

Sequence	Date (UTC)	Time (UTC)	r_h (au)	Δr_h (km s^{-1})	Range (km)	Phase (deg)
MTP12/Deep VAC	2015 Jan 24	11:35 AM	2.47	−12.8	27.9	92.8
MTP14/Deep VAC	2015 Mar 12	1:27 AM	2.12	−13.3	80.7	50.6
MTP15/STP051	2015 Apr 14	4:25 PM	1.88	−13.2	170	74.5
MTP16/STP055	2015 May 12	2:11 AM	1.66	−12.5	155	71.6
MTP17/Deep VAC	2015 June 3	8:04 AM	1.51	−10.9	232	89.3
MTP18/VAC	2015 July 3	8:19 AM	1.34	−7.77	168	89.7

studies must take into account chemical reactions and photolysis to determine how the molecular abundances measured in the coma relate to the bulk composition of the nucleus.

Direct, high-resolution observations of cometary nuclei are rare, and come only from spacecraft encounters. Connecting these measurements to the coma provides a valuable means of evaluating the techniques used in situations where the nucleus cannot be seen. Images obtained by *Giotto*, *Vega*, *Deep Space 1*, and *Stardust* showed details of their targets' nuclei (Keller et al. 1987; Soderblom et al. 2002; Brownlee et al. 2004; Veverka et al. 2013), but in each case, coma observations were limited to the continuum around closest approach. The *Deep Impact* spacecraft was the first to observe both the gas and dust comae of comets 9P/Tempel 1 and 103P/Hartley 2 through a multi-wavelength filter set, while monitoring each comet for months around close approach (A'Hearn et al. 2005, 2011).

Orbiting the comet since 2014 August, the European Space Agency's *Rosetta* mission has allowed an unprecedented study of the activity and evolution 67P/Churyumov–Gerasimenko. The large heliocentric distance of the comet, its low activity levels, and the close proximity of the spacecraft to its surface allow us to sample an environment that has never been studied before and that is not accessible to observers from Earth. This paper describes observations of the dust and gas in the coma of 67P/Churyumov–Gerasimenko acquired by *Rosetta*'s Optical, Spectroscopic, and Infrared Remote Imaging System (OSIRIS). Fragment species are relatively bright and emit in wavelengths accessible from the ground. OSIRIS' narrow-band filters provide an important link to ground-based observations, and help to connect our detailed knowledge of 67P/Churyumov–Gerasimenko to the wider population of comets.

2. OBSERVATIONS

OSIRIS consists of two bore-sighted cameras: a narrow-angle camera (NAC, field of view $2°.2 \times 2°.2$) and a wide-angle camera (WAC, field of view $11°.4 \times 12°.11$) (Keller et al. 2007). The WAC is best equipped to study the coma; its 12 narrow-band and two medium-width filters allow color discrimination and the imaging of emission lines and bands from gas and continuum in optical wavelengths (250–750 nm). We typically monitored gas and dust activity with the WAC, about once every two weeks for heliocentric distances greater than 2 au, and once per week between 2 and 1.3 au pre-perihelion. The nominal sequence had a set of observations once per hour for a full comet rotation (∼12 hr 25 minutes during the observations described here; Keller et al. 2015). As both *Rosetta* and 67P were coming closer to Earth, the data volume available increased, allowing us to increase the observing cadence to one set of observations every 20 minutes, for 14 hr (to avoid aliasing with the comet's rotation period).

Exposure times are optimized to achieve good a signal-to-noise ratio (S/N) in the coma, often resulting in saturation on the nucleus and in the appearance of internal reflection artifacts (ghosts), which appeared on the CCD images as a circular "blob" to the right of the nucleus (Keller et al. 2007). The acquired images are scaled with binning (typically 4×4 for coma observations) and observing geometry (distance to the comet, distance to the Sun). To establish the connection with the nucleus, short-exposure, 2×2 binned images were acquired with the 375 and 610 nm filters along with the coma images. For this paper, we limit ourselves to data acquired during four periods when *Rosetta* conducted the so-called "Volatile Activity Campaigns (VAC)." These campaigns were multi-instrument observations specifically designed to study the gas in the coma of 67P (including OSIRIS, VIRTIS, MIRO, and Alice), and two more dedicated OSIRIS campaigns to provide better temporal coverage. The observations discussed in this article were acquired before the comet's perihelion, between 2015 January 24 and July 3 (see Table 1). During this period, the comet's distance to the Sun decreased from 2.48 to 1.34 au. Because *Rosetta* was close to the surface in January, the nucleus fills a significant part of the field of view, whereas during the later observations the WAC maps a much larger part of the coma. For the analysis described below, we used images acquired at approximately the same diurnal phase.

3. ANALYSIS

3.1. Data Reduction and Image Processing

All images are pre-processed using the standard OSIRIS pipeline (Tubiana et al. 2015), which includes bias and dark subtraction, flat fielding, conversion from electron yield to radiance units (W m^{-2} sr^{-1} nm^{-1}), and bad-pixel masking.

3.1.1. Coma Gas Emissions in the Filters

The narrow-band filters were designed to sample either emission lines and bands of specific gases or continuum light at nearby wavelengths, but inevitably they also sample the emission of other molecules with lines that fall within the narrow-band filters' passbands at various levels. A summary of the characteristics of the WAC's filters and of the most prominent emission features within their passbands is given in Table 2.

The WAC can map the distribution of water with its O I and OH filters. The O I filter covers the forbidden transitions from the O I $(2p^4)$ ^{1}D state to the ground state. The O I $(2p^4)$ ^{1}D state is populated directly by photodissociation of H_2O molecules, as is the O I $(2p^4)$ ^{1}S state, which relaxes mostly (95%) by decay into the ^{1}D state (see Cochran 2008). The OH filter covers the (0–0) band of the A$^2\Sigma^+$ – X $^2\Pi$ transition of OH, centered at about 308.5 nm, which is excited almost entirely by

Table 2
Characteristics of the WAC's Filters (Keller et al. 2007)

Filter + Name	$\lambda_{central}$ (nm)	Width (nm)	Comments
21 Green	537.2	63.2	Includes C_2 Swan $\Delta v = -1, 0$
31 UV245	246.2	14.1	Isolated pinholes
41 CS	259.0	5.6	Several overlapping pinholes. Samples CS $A^1\Pi - X^1\Sigma^+$ (0–0)
51 UV295	295.9	10.9	…
61 OH	309.7	4.1	Several pinholes, one strong (at the lower left quadrant of the CCD images). Samples OH $A^2\Sigma^+ - X^2\Pi^i$ (0–0)
71 UV325	325.8	10.7	Many overlapping pinholes
81 NH	335.9	4.1	Samples NH $A^3\Pi_1 - X^3\Sigma^-$ (0–0). Includes OH^+ ($A^3\Pi - X^3\Sigma^-$)
12 Red	629.8	156.8	Broad-band filter
13 UV375	375.6	9.8	Minor contribution C_3 Comet Head Group
14 CN	388.4	5.2	Samples CN violet system. Minor contribution C_3 Comet Head Group. Includes CO_2^+ ($\tilde{A}^2\Pi_g - X^2\Pi_g$)
15 NH2	572.1	11.5	Samples $NH_2 \, \tilde{A}^2A_1 \to X^2B_1$ (0, 10, 0)
16 Na	590.7	4.7	Covers both Na D1 and D2 doublets; includes C_2 Swan $\Delta v = -2$
17 O I	631.6	4.0	Samples [O I] ^1D–^3P 630 nm line only. Includes $NH_2 \, \tilde{A}^2A_1 \to X^2B_1$ (0, 8, 0)
18 Vis610	612.6	9.8	Includes $NH_2 \, \tilde{A}^2A_1 \to X^2B_1$ (0, 9, 0)

fluorescence of sunlight (see Schleicher & A'Hearn 1988). A small fraction of the photodissociation of H_2O also leads directly to the population of OH in high rotational states of the $A^2\Sigma^+$ electronic state (A'Hearn et al. 2015), but the resulting emission falls outside the passband of the WAC's OH filter. The WAC's CN filter covers emission from $B^2\Sigma^+ - X^2S^+$ (0, 0) transitions around 388 nm. The $NH_2 \, \tilde{A}^2A_1 \to X^2B_1$ (0, 10, 0) band is very wide and how much of the emission falls within the NH_2 filter's passband depends on the heliocentric distance and velocity. The NH filter covers the NH $A^3\Pi_1 - X^3\Sigma^-$ (0–0) transition. While the WAC is equipped with CS and Na filters, those two filters were used only sporadically during the first half of the mission because the low S/N and pinholes (CS) and contamination by C_2 emission (Na) hamper the interpretation of observations made with these two filters.

The WAC is also equipped with several filters that can sample the continuum. Comparing the 375 and 610 nm narrowband filters illustrates the level of contamination of the latter filter by gas emission features. In WAC observations of 16Cyg, a system of two solar analogs, we measured a flux ratio Vis610/UV375 $= 1.648 \pm 0.08$, whereas for the dust surrounding 67P this ratio was between 2.8 and 5.6 (January/March) and 2.5–3.3 (June/July). Such values would require a reddening between 20% and 40% per 100 nm between the two filters, while we determined from the NAC images that the average reddening of the dust between 375 and 610 nm was around 18% per 100 nm (Section 3.1.2.). This suggests that in the January/March data, up to 50% of the flux in the 610 nm filter might come from gaseous emission, probably mostly due to the emission from the $NH_2 \, \tilde{A}^2A_1 \to X^2B_1$ (0, 9, 0) and C_2 $d^3\Pi_g - a^3\Pi_u$ ($\Delta v = -2$) transitions. As will be discussed below, the Vis610/UV375 ratio measured in June and July is close to what is expected based on the NAC reddening measurement, suggesting that the relative contribution of gaseous emission to the flux measured in the Vis610 decreased.

To further assess the gas contamination in other filters, we show the transmission of the WAC filters on a high-resolution spectrum of comet 122P/DeVico (Cochran 2002) in Figure 1 (a). The spectrum of this comet is not a particularly good proxy for that of 67P; the comet was observed very close to the Sun (0.7 au), it was extremely dust-poor, and the two comets have different compositions (67P is depleted in its carbon chain molecules while 122P has a "typical" composition; Fink 2009).
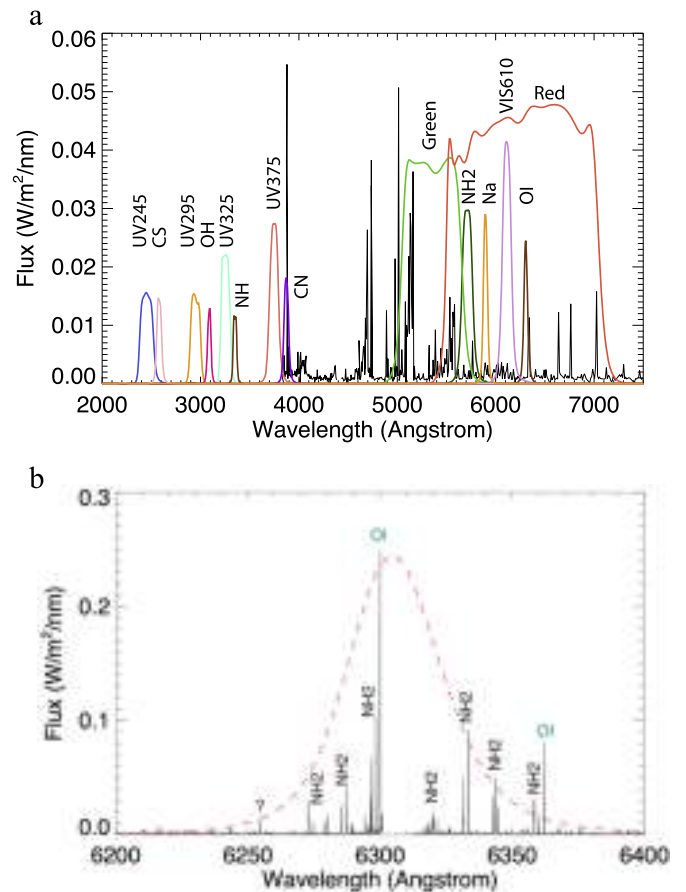
Figure 1. (a) OSIRIS/WAC filter transmission profiles overlaid on a high-resolution spectrum of comet 122P/DeVico (Cochran 2002). Profiles are not convolved with the quantum efficiency of the detector. (b) Enlargement of part (a) for the O I filter transmission.

However, the high-quality spectrum and line catalog demonstrate the extent of the contamination and the identification of the gases responsible for it. An example is shown in Figure 1(b), where we show the transmission of the O I filter overlaid on comet 122P/DeVico's spectrum. The filter was designed to sample emission from the [O I] $^1D \to {}^3P$ line at 630 nm, but also contains several emission lines of the NH_2 molecule, notably the $\tilde{A}^2A_1 \to X^2B_1$ (0, 8, 0). The WAC is equipped with a narrow-band filter designed specifically to

observe the NH$_2$ Ã ^{2}A$_1$ → X ^{2}B$_1$ (0, 10, 0) band, which can be used to remove NH$_2$ emission from the 610 nm (NH$_2$ Ã ^{2}A$_1$ → X ^{2}B$_1$ (0, 9, 0) transition) and O I narrow-band filters (NH$_2$ Ã ^{2}A$_1$ → X ^{2}B$_1$ (0, 8, 0) transition) if the relation between the three different emission bands of NH$_2$ is known. To calculate the contribution of NH$_2$ emission to the flux measured in the NH$_2$, Vis610, and O I filters we weighted the archival spectrum $S(\lambda)$ of 122P with OSIRIS' CCD quantum efficiency $Q(\lambda)$, the reflectivity $R(\lambda)$, and transmission of its filters $T(\lambda)$:

$$S'(\lambda) = \frac{\int Q(\lambda)R(\lambda)T(\lambda)S(\lambda)d\lambda}{\int Q(\lambda)R(\lambda)T(\lambda)d\lambda}. \quad (1)$$

For comet 122P we find that the ratio between NH$_2$ emission in the O I and NH$_2$ filters is 1.389, and the ratio between NH$_2$ emission in the Vis610 and NH$_2$ filters is 0.45. Using this band ratio, we find that NH$_2$ typically contributed between 10% and 20% to the flux measured in the O I filter (after continuum subtraction); however, as we will discuss in Section 5, this assumes that band ratios between photo-fluorescent excitation and electron impact excitation are similar, which may not be the case.

Fluorescence efficiencies for NH$_2$ have been calculated by Kawakita & Watanabe (2002). Their model shows that the ratio between fluorescence efficiencies of even and odd transitions is strongly dependent on the heliocentric distance and heliocentric velocity, but that the ratio between even bands is constant. NH$_2$ emission in the NH$_2$ and O I filters is thus coupled and can be removed with a constant factor that is independent of heliocentric distance and velocity, and this factor should be the same for both 122P and 67P. The Vis610 filter, however, includes emission from an odd band, (0, 9, 0), which has a much more complex relation to the emission in the even (0, 10, 0) band sampled by the NH$_2$ filter. We therefore did not attempt to remove the contribution of NH$_2$ from the images acquired with the Vis610 filter.

In conclusion, we deem the filter centered at 375 nm to be best suited to image the continuum light, although its transmission includes some emission lines from C$_3$ (Ã $^1\Pi_u$ → X$^1\Sigma_g^+$) transitions. There are fewer emission lines at shorter wavelengths, but the three near-UV continuum filters centered on 245, 295, and 325 nm suffer heavily from pinholes (circular defects in the filters' coatings from impurities in the production process), increasing the filter's transmission outside of the intended bandpass. The disadvantage of using the UV375 filter to remove the continuum from all the gas filters is that, since we use only one filter, we do not measure coma colors, and have to assume a linear reflectance with respect to the wavelength. The assumed reddening has a large impact on the continuum removal factor used with increasing wavelength difference.

3.1.2. Continuum Removal and Reddening

To measure the gaseous emission line flux, the contribution of the reflected continuum needs to be removed (see, e.g., Farnham et al. 2000). We used OSIRIS observations of the solar analogues of the 16Cyg system (the two stars are not spatially resolved by the WAC) to determine the ratio of narrow-band continuum fluxes in all filters for a solar spectrum. These ratios a are the weight factors needed to remove the flux contribution of "gray" dust from the total flux F_{tot} measured in a narrow band using the flux F_{375} measured in the UV375 filter

Table 3
Continuum Removal Factors F for the WAC Gas Filters

Filters	Removal Factor				ΔF
	0%	10%	20%	30%	(%)
O I/UV375	1.570	2.026	2.623	3.438	5
CN/UV375	1.021	1.034	1.053	1.077	6
OH/UV375	0.479	0.444	0.397	0.332	10
NH/UV375	0.829	0.790	0.740	0.671	8
NH$_2$/UV375	1.738	2.124	2.630	3.321	5
Na/UV375	1.673	2.080	2.614	3.343	8
Vis610/UV375	1.648	2.127	2.753	3.609	5

Note. These factors assume different continuum reddening (% per 100 nm between 375 and 610 nm). ΔF is the relative, error-propagated 1σ standard deviation of the removal factors.

in order to measure the flux contribution from the gas of interest:

$$F_{gas} = F_{tot} - \alpha F_{375}. \quad (2)$$

The signal-to-noise ratio in the OH and NH filters is poor because UV fluxes from solar analogs are low and the CCD's quantum efficiency drops significantly below 400 nm (Magrin et al. 2015). In addition, the long exposures required in these filters increase the chance of cosmic rays affecting the measurement and reducing the number of usable images. Average filter ratios and 1σ standard deviations are given in Table 2.

To calculate the effect of spectral reddening P (as a percentage per 100 nm) on the flux ratios we first calculated the resulting, reddened spectrum by weighting a solar spectrum with the reddening $R(\lambda)$ as a linear function of wavelength λ between $\lambda_1 = 375.6$ nm and $\lambda_2 = 612.6$ nm (the central wavelengths of two of the WAC's continuum filters), normalized at 494 nm:

$$R(\lambda) = 1 + 0.01P[\lambda - 0.5(\lambda_2 - \lambda_1)]. \quad (3)$$

We used the ratios of the fluxes of the reddened spectrum and the original solar spectrum to calculate continuum removal factors for increasing reddening, which are given in Table 3. To estimate the average reddening of the continuum of 67P we performed a deeper investigation of the colors of the coma using observations with the NAC medium-band filters, for which the contributions of extraneous emission lines should be less important. For this, we chose a data set that had good coverage of the coma around the nucleus and used a large number of filters. The selected images were acquired on 2015 February 18 in five filters: near-UV, blue, orange, red, infrared. The comet was at about 2.3 au from the Sun and the phase angle was about 85°. The spacecraft was at 220 km from the comet and the NAC's field of view was about 9 km around the nucleus.

We constructed a map of radial distance from the limb of the nucleus and computed the average surface brightness of the coma over an azimuthal region generally free of gas jets and ghosts. Assuming that in the broad NAC filters (mostly ~50 nm) the contribution of the gas emission is small with respect to the dust contribution, we derived the colors of the dust coma. We found that the coma has an average reddening of 19% per 100 nm in the wavelength range 360–649 nm, the closest to the 375–610 nm range obtained with WAC filters.

Table 4
Photon Production Efficiencies Based on Photodissociation Rates (O I) and Fluorescence Models (OH, CN, NH) in Units of Photons/molecule

Date	O I[1]	OH[2] (photons molecule^{-1} s^{-1})	CN[3]	NH[4]
2015 Jan 14	9.95×10^{-8}	7.13×10^{-5}	0.010	1.89×10^{-3}
2015 Mar 12	1.35×10^{-7}	9.21×10^{-5}	0.014	2.56×10^{-3}
2015 Apr 14	1.72×10^{-7}	1.18×10^{-4}	0.018	3.29×10^{-3}
2015 May 12	2.20×10^{-7}	1.61×10^{-4}	0.023	4.20×10^{-3}
2015 Jun 3	2.85×10^{-7}	1.95×10^{-4}	0.029	5.09×10^{-3}
2015 July 3	3.59×10^{-7}	1.43×10^{-4}	0.041	6.68×10^{-3}

References. (1) Bhardwaj & Raghuram (2012), (2) Schleicher (2010), (3) Schleicher & A'Hearn (1988) and Kawakita & Watanabe (2002), (4) Kim et al. (1989).

However, NAC imaging is not available concurrently with most WAC gas observations, and it may or may not sample the relevant region of the coma given the instrument's small field of view. Therefore, we devised a second, empirical method to determine the reddening of the dust in the coma. We assumed that NH_2 emission comes predominantly from fragment species in the coma. Thus, for the images of 67P acquired with the NH_2 filter the underlying continuum subtraction was done by varying the continuum removal factor until jets disappeared from the NH_2 filter image, leaving a rather isotropic NH_2 coma. This method typically yields factors that correspond to 17%–20% per 100 nm between 375 and 610 nm, somewhat larger than reported from ground-based observations of the comet in previous appearances ((11 ± 2)% per 100 nm between 436 and 797 nm; Tubiana et al. 2011) but consistent with ground-based observations acquired during this appearance (20% between B and V; Snodgrass et al. 2016). We therefore used a constant reddening of 18% per 100 nm for the data discussed in this paper.

3.2. Column Densities and Production Rates

We identified observations in each sequence that were acquired at the same diurnal phase, extracted surface brightness profiles in two directions, and measured the surface brightness at a fixed position 3 km in the sunward direction above the surface.

When the formation and excitation processes of the fragment species are known, the measured surface brightnesses $S(x, y)$ can be converted into column densities N_{col} by assuming fluorescence efficiencies g of each species:

$$N_{col}(x, y) = \frac{4\pi S(x, y)\Delta\lambda}{E_p g}, \qquad (4)$$

where $\Delta\lambda$ is the FWHM of the filter (Table 2) and E_p the energy of the photons at the wavelength of the emission feature considered. [O I] surface brightnesses can be converted into H_2O column densities using reaction rates for prompt excitation of the ^1S and ^1D states (Bhardwaj & Raghuram 2012), weighted by the branching ratios of the transitions leading to emission at 630 nm (the second line of the doublet at 636 nm is at the edge of the O I filter where the transmission is below 6% of the peak transmission; see Figure 1(b)). The CN, OH, and NH surface brightnesses were converted into column densities using published fluorescence

efficiencies (Table 4). We have calculated production rates using a standard Haser model for easier comparison with other observations. Assumed outflow velocities and lifetimes for parents and daughters can be found in the Appendix (Table 7). To better evaluate the column densities, we also calculated production rates with a modified Haser model that takes into account the gas acceleration, collisional quenching of the long-lived ^1D state of the oxygen atom, and the effect of the oxygen atom moving out of the field of view before it can decay to the ground state. This model is described in the Appendix.

3.3. Uncertainties

The results are subject to several possible systematic uncertainties. The absolute calibration of OSIRIS is better than 1% for most filters, but the calibration constant for the OH filter (and continuum filters <300 nm) has an uncertainty of ∼10% (Tubiana et al. 2015). Bias levels are temperature-dependent and have gradually changed over time because the spacecraft approached the Sun. From the 16Cyg observations (where we can see the background), we estimate that the bias level is now constrained to within 1 DN (digital number).Because the bias is individually determined for each hardware configuration, the error remains 1 DN independent of binning. The resulting gas detections typically had a S/N of 4 or better per 4×4 pixel at 100 pixels from the nucleus. The continuum removal is the largest systematic and statistical uncertainty in our data analysis. For example, in the data acquired in March, at a distance of 100 pixels, i.e., 0.82 km, from the nucleus, the continuum contributes 10% to the total signal in CN, ∼20% in O I, ∼30% in OH, and as much as 65% of the signal in the NH_2 filter. We have also tried to optimize the quality of the continuum removal factors by averaging repeated observations of 16Cyg, and these coefficients are now constrained within 5%–10% (Table 3). As discussed above, we only use the UV375 filter to observe the continuum emission, and have to infer the color of the coma. We do not account for spatial gradients and temporal variations in the color of the coma. Assuming that the reddening is typically between 0% and 30%, differences in reddening could result in uncertainties of <1% (CN), 8% (O I), 5% (OH), and 30% (NH_2) in the resulting pure gas emission after continuum subtraction.

Uncertainties in the assumed fluorescence efficiencies can affect the results systematically. Moreover, the use of those factors rests on the premise that the dominant processes are photo-processes, which we deem not be the case (Section 5).

4. RESULTS

Narrow-band images for March and June after removal of continuum and contaminants are shown in Figure 2, along with contextual images acquired with the 375 nm filter. All images are oriented such that the direction to the Sun is upward. In each frame, the entire field of view of the WAC is shown, the sides of which correspond to 16 and 46 km projected at the distance of the nucleus. In each image a circular feature can be seen on the right side of the nucleus (saturated pixels are masked black in our image processing). These "ghosts" are caused by internal reflections from optical elements and always occur at the same place on the detector with respect to the nucleus. A smaller, weaker artifact can be seen in the same direction directly next to the nucleus. Three remnant pinholes can clearly be seen in the OH images.
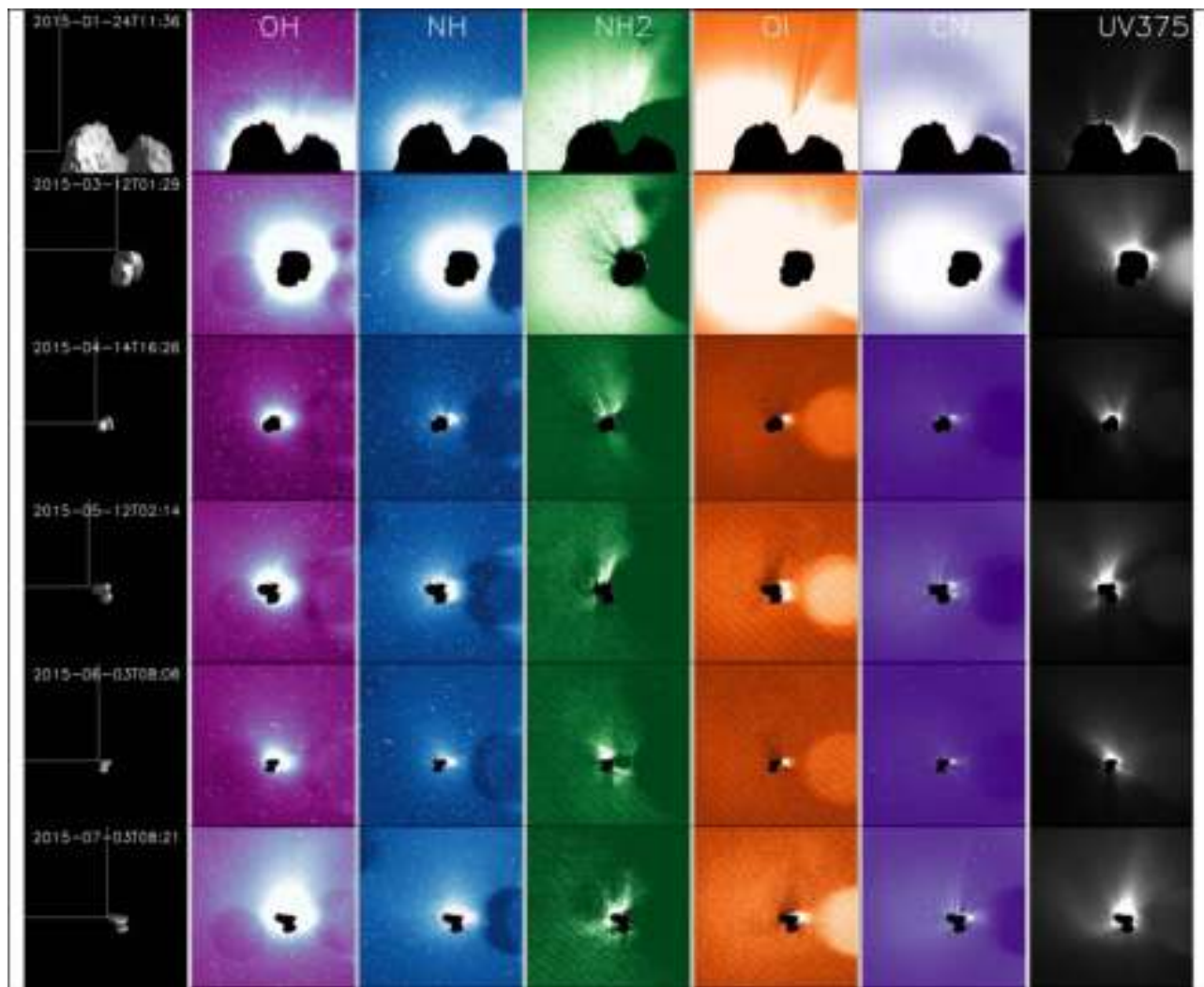
Figure 2. Left to right: model image of the comet nucleus for reference, continuum-subtracted images acquired with the OH, NH, NH₂, O I, and CN filters, and a long-exposure UV375 filter image for comparison. In the orientation used here, the Sun is always toward the top, and the main reflection ghost can be seen to the right of the nucleus. A smaller artifact can be seen immediately right of the nucleus. All images are the entire field of view of the WAC ($11°4 \times 12°1$). The color scale is different for every filter, but is kept constant throughout all epochs within each filter.

All continuum images show multiple bright, collimated jets on the sunward side of the nucleus. In the top row (the March data) those jets are not present in any of the continuum-subtracted gas images. At all epochs we see a plume-like morphology perpendicular to the sunward direction. This feature is seen in the O I and CN filter, but not in the OH, NH, and NH₂ filters, where the observed morphology is less pronounced and is enhanced toward the Sun (Figure 2).

The continuum-subtracted NH₂ images have poor S/N and show a broad distribution with little structure. For the data acquired in June and July, while assuming the same reddening of 18% per 100 nm (Section 3.1.2), the jets are oversubtracted in the O I data and cannot be entirely removed from most of the other filters. We believe this to be a consequence of our approach to the continuum subtraction (i.e., assuming a constant color throughout the inner coma). For each of the images in Figure 2, the color scale of the lookup table was adjusted to best emphasize the morphology. It is clear that while the morphology in the OH and NH images remains isotropic and diffuse, the cone in the [O I] and CN images becomes much fainter and less defined over time.

Radial surface brightness profiles were extracted from a 21 pixel wide box between the left limb of the nucleus and the edge of the frame. We extracted surface brightnesses in both the horizontal and vertical (sunward) directions, starting at the nucleus (orientation as in Figure 2). The 1σ uncertainty was estimated from the standard deviation within the 21 pixel wide box. The resulting continuum-subtracted profiles are shown in Figure 3. The first two epochs show the best S/N. The surface brightness decreased by a factor of 5–10 after February, resulting in visibly poorer S/N. For the observations in April, May, and June, data within 1 km from the surface seem unreliable, with the exception of CN. NH₂ is consistently very noisy (the plots have a logarithmic scale so negative values are not shown), and it was probably not detected in 2015 June and July. At all six epochs, there is a clear difference between the shapes of the profiles of OH and NH, which show a $1/r$ drop-off with distance, and those [O I] and CN, which are flat within the first ~8 km from the surface. In January and March, the OH profiles in the sunward direction are very similar to those in the perpendicular direction. After that, the emission on the sunward side of the coma is much stronger (by a factor of 2) than that in
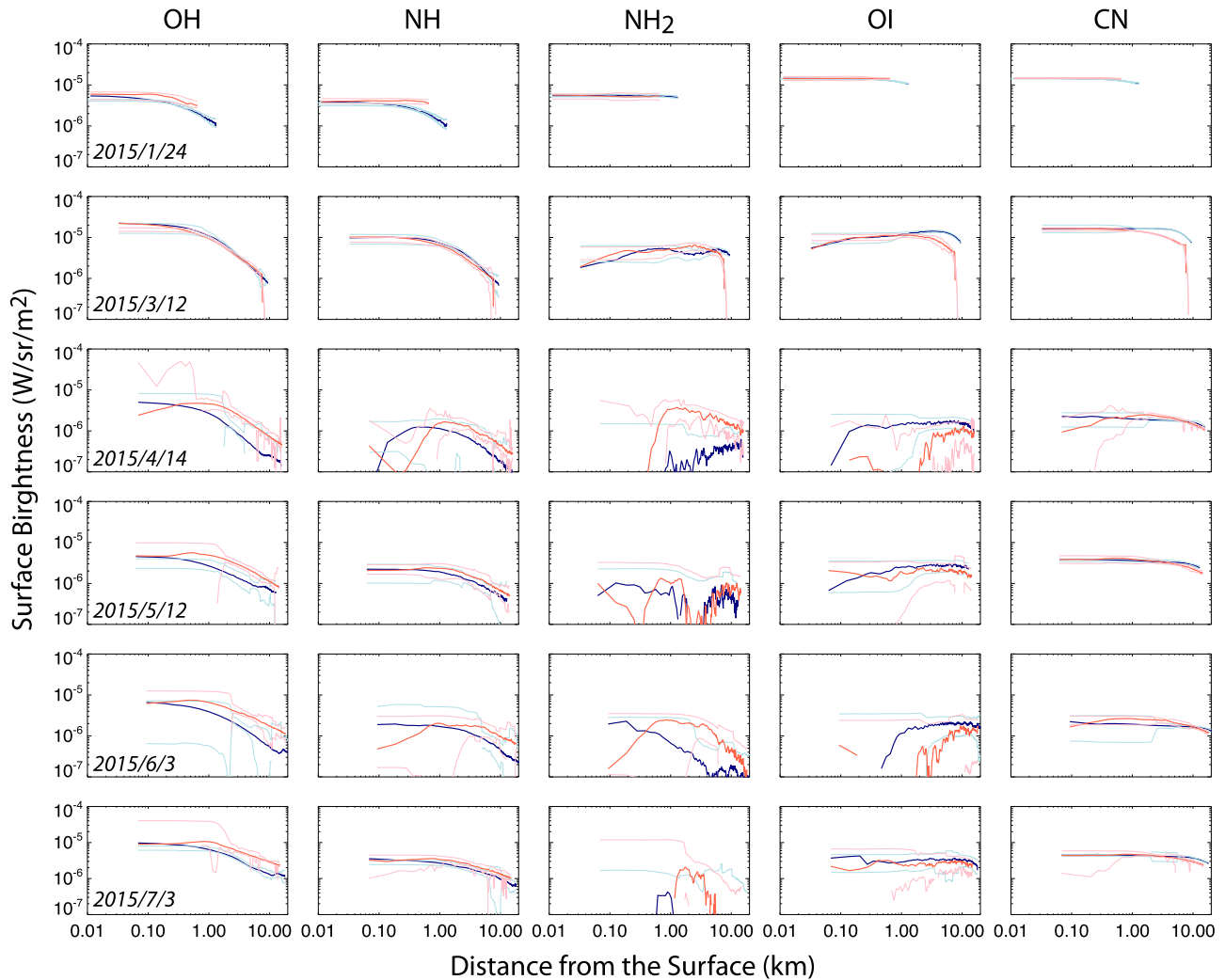
Figure 3. Surface brightness profiles. Blue lines are profiles in the horizontal direction ("plumeward"); red lines are profiles in the vertical direction (sunward; see Figure 2). The thin lines in lighter shades (pink and cyan) indicate the 1σ uncertainties.

the direction orthogonal to the comet–Sun line. This asymmetry is also present in the NH profiles, albeit less pronounced. In the O I and CN profiles, the emission is somewhat stronger in the orthogonal direction because the plumes visible in Figure 2 extend in both extraction directions. At the two epochs where we have a good NH_2 detection, January and March, the profiles are very flat and very different from the NH profile.

5. EMISSION PROCESSES

There are numerous inconsistencies in our results if we assume standard cometary physics. First, column densities and production rates derived from OSIRIS images are much higher than those measured by other instruments on board *Rosetta* (MIRO, VIRTIS, and ROSINA/COPS; Bieler et al. 2015a; Bockelée-Morvan et al. 2015; Fougere et al. 2016). Assuming photodissociation of H_2O as the main source of formation and prompt emission by atomic oxygen, and photodissociation and subsequent fluorescent excitation of OH, CN, and NH emission, we derived column densities and calculated global production rates using the standard Haser model (Figure 4, Tables 5 and 6).

There are currently no contemporaneous measurements available of the abundance of CN and NH. Abundances of

NH_3 and HCN were 0.06% and 0.09% with respect to water, measured by *Rosetta*'s ROSINA instrument at 3.1 au on the sunward side of the comet (Le Roy et al. 2015). Fink (2009) measured NH_2 and CN abundances of 0.19% and 0.15% from the ground at 1.35 au from the Sun post-perihelion during the 1995 apparition. To calculate the expected surface brightness levels, we assumed abundances of 0.1% for HCN and NH_3, and water production rates from Fougere et al. (2016). As shown in Figure 4(a), water production rates derived from the OH observations using the standard Haser model are initially more than a factor of 300 larger than expected. Production rates derived from CN and NH surface brightnesses are also larger by factors of 1000. This changes dramatically when we assume a more realistic velocity (Equation (8)) in the inner coma, see Figure 4(b). Production rates for H_2O derived from OH are now about one order of magnitude too large, and those of NH and CN parents about two orders of magnitude too large. For OH and CN, the July results are consistent with expected production rates. NH emission remains about a factor of 10 too high.

Second, with the WAC we expect to observe two water photolysis products, OH and O I. Using the standard Haser model, water production rates derived from OH seem
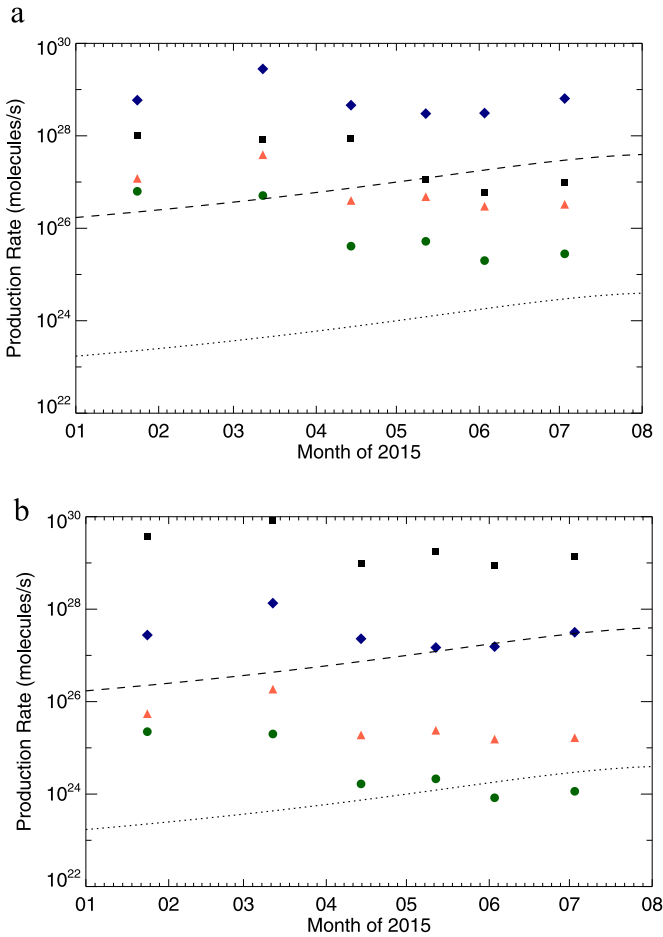
Figure 4. (a) Water production rates derived from OH (blue diamonds) and [O I] (black squares), CN production rates (green circles), and NH production rates (red triangles), based on the assumption that photodissociation and fluorescence are the driving destruction and excitation mechanisms. The dashed line indicates H_2O production rates derived from MIRO measurements (Fougere et al. 2016); the dotted line indicates expected production rates of NH_3 and HCN assuming fixed abundances of 0.1%. (b) As for part (a) but production rates are now calculated using an enhanced model that includes acceleration in the inner coma. H_2O production rates derived from [O I] emission include quenching and transport effects.

significant vectorial kick upon photodissociation of a parent species. The morphology of emission in the O I and CN images resembles the projection of a cone of gas and indicates a parent dissociation process that produces these fragments directly into an excited state.

We therefore conclude that by adjusting our models to better describe the physical processes in the inner coma we can explain some of the observations, but that the differences between our observations and model results indicate that photodissociation and fluorescence are not the dominant processes resulting in the OH, [O I], CN, and NH emission observed in the inner coma. Instead, the fragments might be fragments from different parent species and/or formed by other processes. We will discuss this in more detail below.

5.1. Water Fragments: OH and O I

As concluded above, the emission from O I and OH cannot be explained by photodissociation of H_2O, followed by prompt emission of O I or by fluorescence of OH. The surface brightness profile of OH suggests that its emission might be the product of a process that produces OH directly in the $A^2\Sigma^+$ state. However, the difference between the [O I] and OH morphology indicates that at least part of the emission of the two fragments is not related.

From the morphology of the [O I] emission we concluded that it is the product of a process that directly produces atomic oxygen in an excited state. Like H_2O, photodissociation of CO_2 and CO produces O I in the ^1D and ^1S states, resulting in [O I] emission at 630 nm. Abundances of CO_2 and CO vary greatly between the summer and winter hemispheres. Here we assume that the sunlit side dominates the total gas production rate; there, abundance ratios from the "summer hemisphere" apply, which are $H_2O:CO_2:CO = 100:2.7:2.5$ (Le Roy et al. 2015). Assuming formation rates of O I ^1D and ^1S from CO_2 and CO from Bhardwaj & Raghuram (2012), photodissociation of CO_2 and CO contributes 10% and <1% to the [O I] 630 nm emission compared to H_2O (100%).

The ROSINA instrument reported unexpectedly high abundances of O_2, with an average of $O_2/H_2O = (3.7 \pm 1.5)\%$, with local abundances as high as 10% (Bieler et al. 2015b). The distribution of O_2 in the coma suggested that it is released by the nucleus and that its release is correlated to the outflow of water. Because the photodissociation of O_2 into O I ^1D is very efficient at these abundances (Huebner et al. 1992), it can contribute as much as an additional 25%–60% to the [O I] 630 nm emission from H_2O. Thus while the photodissociation of CO_2, CO, and O_2 molecules combined may produce as much [O I] emission as the photodissociation of H_2O, it cannot explain the factors of 20–40 of flux excess observed between January and March, nor can it explain the OH observations.

We then considered several processes that might produce the high observed surface brightness of both OH and [O I] directly from H_2O, including dissociative recombination of H_2O^+, electron excitation of O I, and sputtering of water ice (see Bhardwaj & Raghuram 2012) but none of those have reaction rates that exceed that of photo-processes. Feldman et al. (2015) concluded that electron impact dissociation of H_2O vapor produced H I and O I emission observed by *Rosetta*/Alice in the far-UV. Electron impact dissociation produces O I in the ^1D and ^1S states, and OH in the $A^2\Sigma^+$ state. Those reactions typically have appearance thresholds between 10 and 20 eV,

consistently larger than those derived from [O I], by a factor of 6 in January and by a factor of 30 in July. This situation is not resolved by our appended coma model because there is no change in the relative column densities of OH and O I if both are assumed to come from H_2O.

Third, all production rates drop significantly between 2015 March and June. This variation is much larger than the diurnal variation of the total water production (~25%; Gulkis et al. 2015) and not consistent with the observed trend of increasing production rates with decreasing heliocentric distance.

Fourth, the luminosity profiles are at odds with the observed morphology. Surface brightness profiles of parent species usually decrease with $\sim 1/r$ close to the nucleus, whereas those of fragment species have shallower slopes (see Combi et al. 2004). The OSIRIS surface brightness profiles (Figure 3), however, are flat for [O I] and CN, for which the morphology suggests a prompt excitation process. In contrast, the morphology seen in the OH and NH filters—a symmetric distribution around the nucleus—is typical for a fragment species that gets a

Table 5
Surface Brightness Measured at 1 km above the Surface in the Horizontal Direction (Orthogonal to Sunward Direction)

Date	Surface Brightness (10^{-6} W m^{-2} sr^{-1})					Log(Column Density) (molecules m^{-2})			
	O I	OH	CN	NH	NH$_2$	O I	OH	CN	NH
2015 Jan 24	11.5 ± 0.2	1.5 ± 0.2	11.4 ± 0.2	1.4 ± 0.2	5.3 ± 0.3	21.7	17.6	16.5	16.2
2015 Mar 12	12.1 ± 1.0	11.0 ± 1.3	16.5 ± 0.2	7.4 ± 0.5	4.8 ± 1.4	21.6	18.4	16.5	16.8
2015 Apr 14	1.3 ± 0.8	2.7 ± 0.2	2.0 ± 0.1	1.1 ± 0.8	0 ± 1	20.5	17.6	15.4	15.9
2015 May 12	2.4 ± 0.9	2.7 ± 0.4	3.7 ± 0.2	2.0 ± 0.5	0.9 ± 1	20.6	17.5	15.6	16.0
2015 Jun 03	1.6 ± 1.0	3.8 ± 0.2	2.0 ± 0.3	1.7 ± 0.5	0.8 ± 0.8	20.1	17.6	15.2	15.8
2015 Jul 03	3.1 ± 1.6	6.4 ± 0.3	4.4 ± 0.3	2.7 ± 0.3	1.1 ± 2	20.5	17.9	15.4	15.9

Note. Column densities and production rates are derived assuming photo-processes and are given only to show the discrepancy between observations and expected production rates (Section 5).

suggesting that they are driven by the large population of suprathermal electrons observed in by *Rosetta*'s Ion and Electron Sensor (IES; Clark et al. 2015). While electrons with energies of 100 eV and larger were observed, the distribution falls off steeply above 30 eV. At these impact energies, the cross section for electron impact production of OH ($A^2\Sigma^+$) is 7×10^{-22} m^2 (Avakyan et al. 1998) and that of O I (^{1}S+^{1}D) is 6×10^{-23} m^2 (Bhardwaj & Raghuram 2012).

To test whether electron impact dissociation can explain the observed surface brightness we added electron impact processes to our model (see the Appendix). In brief, we assumed a spherically outgassing nucleus with water production rates from the empirical trend reported by Fougere et al. (2016), and relative abundances of 3% for CO and CO$_2$, and 0.1% for HCN and NH$_3$. For the electrons, we assumed a radial distribution that decreased with the inverse of the distance to the nucleus based on measurements by the *Rosetta* Plasma Consortium's (RPC) Langmuir Probe and Mutual Impedance Probe. For the electron density, we used measurements with the IES (Broiles et al. 2016), which we assumed to increase linearly with the production rate and quadratically with the decrease in heliocentric distance. In addition, we included the effects of quenching of the O I ^{1}D state by collisions with H$_2$O molecules as well as the effect of transport as the O I atom moves out of the field of view before it can decay to the ground state.

The results of the model are shown in Figure 5. We find that at 1 km from the surface, electron impact dissociation of H$_2$O can produce up to a factor of 10 more [O I] 630 nm emission than the photodissociation of H$_2$O into excited O I ^{1}D, and at least two orders of magnitude more OH emission than the photodissociation of H$_2$O and subsequent fluorescent excitation of OH by sunlight. However, the morphology and surface brightness profiles seen in the O I and OH filters are very different, which is surprising since we assumed that they are both the product of electron impact dissociation of H$_2$O. In the O I images there is a clear plume visible to the left, which is entirely absent from OH images. If the main emission in the plume originated from electron impact dissociation of H$_2$O, it should also be present in OH emission. If electron impact dissociation drives the emission of [O I] and OH in the coma, then the atomic oxygen emission in the plume is probably produced from a molecule other than H$_2$O.

We are not aware of experimental cross sections for the production of O I (^{1}D), but Bhardwaj & Raghuram (2012) suggest, based on theoretical cross sections, that reaction rates for producing O I (^{1}D) from CO$_2$ are as much as 40 times larger than reaction rates for producing it from H$_2$O. The reaction

rates for the production of excited oxygen atoms from CO are much lower than those for H$_2$O. Assuming these cross sections for electron impact dissociation, a CO$_2$/H$_2$O abundance of 3% would imply that 60% of the observed [O I] emission comes from CO$_2$. This large contribution by electron impact dissociation of CO$_2$ explains the differences between both the morphology and surface brightness profiles of the [O I] and OH emission. The plume is visible in [O I] but not in OH. Its [O I] surface brightness at the core is about twice that at similar distances in the ambient coma, suggesting a local enhancement of the CO$_2$ abundance.

We do not expect our model to provide a fully realistic description of the inner coma. Predicted OH surface brightnesses are higher than observed, and quenching and transport may reduce the detectable [O I] surface brightness by as much as a factor of 100 (Figures 5(a) and (c)). In particular, the asymmetric outgassing of 67P will affect the impact of these processes. However, our results do confirm that electron impact dissociation can indeed explain the emission observed in OSIRIS' O I and OH filters from 2015 January through April.

5.2. Ammonia Fragments: NH and NH$_2$

The photodissociation of NH$_3$ results in the production of NH$_2$ (96%) and NH (~3%); most of the NH is thus normally a granddaughter product of NH$_3$ (Huebner et al. 1992). Electron impact dissociation of NH$_3$ has been relatively well studied and cross sections for the production of NH$_2$ ($\tilde{A}$ ^{2}A$_1$) and NH (A$^3\Pi_1$) at 100 eV are both ~(2–3) $\times$ 10^{-22} m^2 (Müller & Schulz 1992), i.e., three times smaller than the production of excited hydroxyl from H$_2$O (Table 7). To our knowledge, a detailed study of the excitation of NH$_2$ through this process is not available, leaving the relative intensities of the NH$_2$ bands that contaminate several filters an open question (Section 3.1.1). Surprisingly, the surface brightness profiles of NH$_2$ and NH are very different (Figure 3), which is inconsistent if the emission from both fragments is produced by electron impact dissociation of NH$_3$. We used our model to evaluate the surface brightness expected from different emission processes. In all observations, the profile of NH resembles that of OH, suggesting that the same physical process causes the emission. The profile of NH$_2$ resembles that of [O I] and CN in January and March, and was probably not detected after that.

Assuming an abundance of 0.1% with respect to H$_2$O, we included electron impact excitation and fluorescent emission in our model. Photodissociation of NH$_3$ into NH$_2$ and NH cannot explain the emission for any of the observations (Figure 4(b)), nor does electron impact dissociation (Figure 5(c)), both of

Table 6
Production Rates Derived Assuming Photo-processes

| | Standard Haser | | | | Enhanced Model | | | | |
| | Log(Prod. Rate) (molecules s^{-1}) | | | | Log(Prod. Rate) (molecules s^{-1}) | | | | |
Date	O I	OH	CN	NH	O I[a]	O I[b]	OH	CN	NH
2015 Jan 24	28.0	28.8	26.8	27.1	27.7	29.6	27.4	25.4	25.7
2015 Mar 12	27.9	29.5	26.7	27.6	27.6	29.9	28.1	25.3	26.3
2015 Apr 14	27.9	28.7	25.6	26.6	26.6	29.0	27.4	24.2	25.3
2015 May 12	27.1	28.5	25.7	26.4	26.7	29.2	27.2	24.3	25.4
2015 Jun 03	26.8	28.5	25.3	26.5	26.5	29.0	27.2	23.9	25.2
2015 Jul 03	27.0	28.8	25.5	26.5	26.7	29.1	27.5	24.1	25.2

Note. These rates are given only to show the discrepancy between observations and expected production rates (Section 5). Results are shown for a standard Haser model, for an enhanced model that includes acceleration (O I[a]), and for a model that includes quenching and transport of O I (O I[b]). The production rates are all for the assumed parents of the observed fragments; the label indicates from what fragment they were derived (i.e., O I for H_2O, OH for H_2O, CN for HCN, and NH for NH_3).

which fall short by about a factor of 100. Upon further investigation, the only plausible explanation for the NH filter observations appears to be emission from the OH$^+$ (A$^3\Pi$ – X$^3\Sigma^-$ 0–0) band. Electron impact dissociation on H_2O can indeed produce excited hydroxyl ions with a cross section of 8×10^{-24} m^2 at 100 eV (Müller et al. 1993), or about 100 times smaller than that for the production of OH (A$^2\Sigma^+$). The emission cross sections for the production of neutral and ionized OH from H_2O both depend strongly on the electron impact energy, and the ratio between the surface brightnesses in the NH and OH filters will therefore depend strongly on the electron temperature in the coma.

5.3. CN

The morphology of the CN emission resembles that of [O I] at all six epochs, and like the water fragments, its surface brightness is higher than expected from photo-processes, by as much as a factor of at least 200 (Figure 4(b)). Prompt excitation of CN following photodissociation of HCN is not a very efficient emission mechanism (Bockelée-Morvan & Crovisier 1985; Fray et al. 2005), and our model indeed suggests that photodissociation of HCN and subsequent fluorescent excitation of CN would produce at least 50 times more light than prompt excitation of CN following the photodissociation of HCN. Following the discussion on the production of [O I] and OH emission, we then evaluated whether electron impact dissociation of HCN into the CN (B$^2\Sigma$) state can drive the production of excited CN. Qualitative results confirm that this reaction channel is important in electron impact dissociation of HCN (Nishiyama et al. 1979), but cross sections are not available in the literature. Assuming cross sections and abundances similar to NH_3 reactions for HCN, we would expect surface brightnesses comparable to NH in January (Figure 5(c)), i.e., around 10^{-8} W m^{-2} sr^{-1} at 1 km from the surface. Interestingly, owing to the large fluorescence efficiency of CN, emission levels from the photodissociation of HCN followed by fluorescent excitation of CN likely produce an order of magnitude more light than electron impact dissociation of HCN. Dissociative electron impact excitation of HCN cannot explain our observations.

This suggests that the light observed in the CN filter in January is produced by another species. According to Ajello et al. (1971) about 5% of the light emitted following ionizing electron impact excitation of CO_2 falls within the CN filter's passband. This also explains the similarity in morphology

between the O I and CN filter images. At an impact energy of 30 eV, the emission cross section for the entire CO_2^+ (Ã$^2\Pi$ – X$^3\Sigma^-$) band is 4×10^{-21} m^2, thus resulting in an emission cross section of 2×10^{-22} m^2, about four times smaller than that of dissociative electron impact excitation of H_2O into OH*, and about 10 times smaller than that for the production of O I ^{1}D from the dissociative electron impact excitation of CO_2. We note that the [O I] emission is strongly affected by quenching and the effect of transport but the CO_2^+ emission is not, which may explain why [O I] surface brightnesses are comparable to those measured in the CN filter (Table 5). The expected CO_2^+ surface brightness can be estimated from the CO_2-to-[O I] profile in Figure 5(a) and will be of the order of 10^{-5} W m^{-2} sr^{-1}, or about 100 times that of fluorescent emission from CN. Photodissociation of a parent molecule and subsequent fluorescent excitation of fragment CN can explain the observed surface brightness levels after 2015 May, but the persistent plume morphology suggests that the observed emission may be a product of both CN fluorescence emission and CO_2^+ emission from electron impact.

6. TRENDS WITH PERIHELION DISTANCE

The production rates shown in Figure 4 suggest three different epochs: increasing emission before 2015 March following the heliocentric trend observed by MIRO, then a sharp decrease between mid-March and June, followed by an increase after 2015 June. The drop in coma emission is more than an order of magnitude and is seen in the O I, OH, CN, NH, and NH_2 filters. Over the course of our observations, the morphology of the emission in the different filters does not change noticeably (Figure 2). After May, the OH and CN emission levels are as expected from photo-processes alone (Figure 4). If the electron density evolved with our scaling law (linearly with the gas production and inverse quadratically with the heliocentric distance), we would expect 1000 times more OH emission than was observed (Figure 5(d)). Similarly, the predicted [O I] emission from dissociative electron impact of H_2O and CO_2 would produce 10 times more emission than was observed in July. However, production rates derived from [O I] and NH surface brightnesses assuming photodissociation are still unrealistically high (Figure 4), and the morphology in the CN filter still resembles that seen in the O I filter, suggesting that collisions with electrons still play a role in the emission observed after 2015 May. We propose that the drop between March and June 2015 was thus caused by a change in the
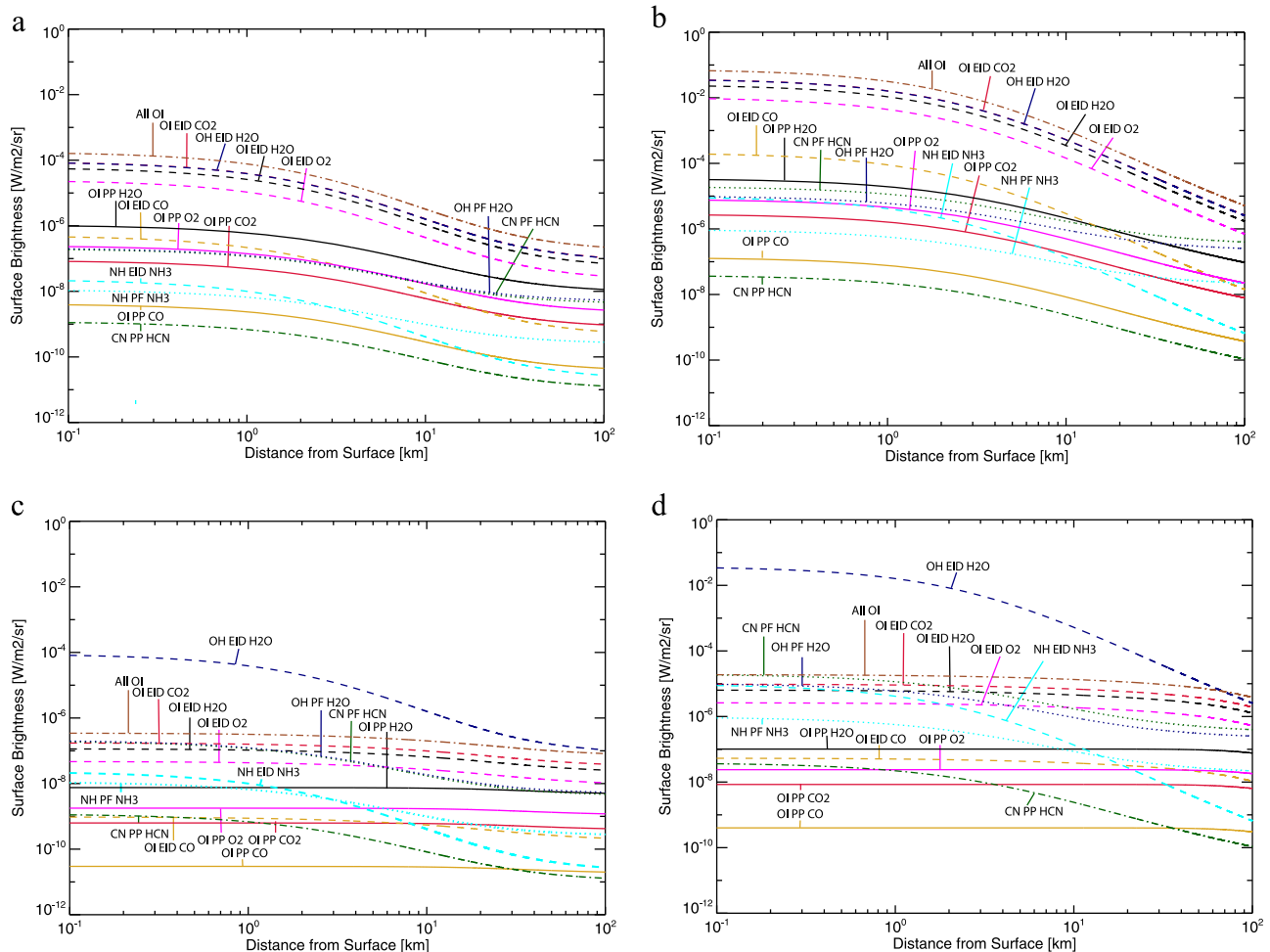
Figure 5. (a) Modeled surface brightnesses from different processes in the coma for the 2015 January 24 observations. EID—electron impact dissociation (dashed lines). PP—photodissociation, prompt excitation (solid lines). PF—photodissociation and subsequent fluorescent emission (dotted lines). Colors indicate the parent species: black and blue—H_2O products; red—CO_2 products; orange—CO products; magenta—O_2; green—HCN; cyan—NH_3. The dashed–dotted brown line shows the sum of all [O I] emission. (b) As for part (a) but for the 2015 July 3 observations. (c) Modeled surface brightnesses from different processes in the coma for the 2015 January 24 observations, but including the effect of collisional quenching and transport. EID, PP, PF, and all colors and lines are coded as for part (a). (d) As for part (c) but for the 2015 July 3 observations.

number or temperature of projectile electrons available, and that this affects the emission in the different filters in different ways, according to the energy dependence of the relevant electron impact dissociation processes.

To explain the decrease in emission, we first consider the production of electrons. The *Rosetta*/RPC observations in 2015 February indicate that the main source of electrons within 256 km of the nucleus is the neutral gas in the coma (Edberg et al. 2015). The far- and extreme-ultraviolet (FUV/EUV) solar flux determines the photoionization rates of H_2O and other molecules in the coma, and thus also controls the number of electrons available. Daily averaged solar UV spectra are available from the Extreme Ultraviolet Variability Experiment on board the *Solar Dynamics Observatory* (*SDO*/EVE; Woods et al. 2012). We integrated the irradiance spectra over the range 30–100 nm,[29] the wavelengths that are most efficient in producing electrons by ionizing water (Huebner et al. 1992; Budzien et al. 1994). The results are shown in Figure 6(a). Over the course of our observations, the UV irradiance

decreased gradually, and it varied by 10% on timescales of one or two weeks. Comparing the production rates and UV irradiances in Figure 6(a) suggests that there is no clear correlation between the short-term solar variations. In this period the comet approached the Sun from 2.5 to 1.3 au, an effect much larger than the weekly UV variations.

With increasing gas production rates, the optical depth of the inner coma increases and fewer photoelectrons are produced. To investigate the optical depth of the coma, we calculated H_2O column densities using a Haser distribution (see the Appendix), and assumed water production rates from the empirical formula by Fougere et al. 2016; Figure 4). The dominant photons for ionization have wavelengths between 30 and 85 nm (Huebner et al. 1992; Budzien et al. 1994). At these two wavelengths, H_2O has photoabsorption cross sections of 1.0×10^{-21} m^2 and 1.6×10^{-21} m^2, respectively (Phillips et al. 1977). The results are shown in Figure 6(b). The relevant region here is between 1 and 10 km from the surface. In January, only 1%–10% of photons were lost within this region. This increased to 10%–64% in July. The electron production thus likely decreased in the region seen by OSIRIS, but not by enough to explain the observed drop in emission.

---

[29] We used data from *SDO*/EVE level 3 version 5 acquired with the MEGS-B instrument, which are available online at http://lasp.colorado.edu/eve/data_access/evewebdata/products/level3/.

Table 7
Assumed Reaction Rates (at $r_h = 1$ au) and Cross Sections

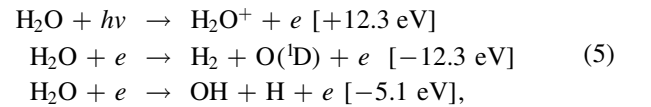| Reaction	Product	Cross section or rate	Reference
$H_2O + hv$	any	1.04×10^{-5} s^{-1}	Combi et al. (2004)
$H_2O + hv$	$OH + hv$	8.5×10^{-4} s^{-1}	Combi et al. (2004)
$H_2O + hv$	O I ($^1S + {}^1D$)	8.6×10^{-7} s^{-1}	Bhardwaj & Raghuram (2012)
$CO_2 + hv$	any	2.2×10^{-6} s^{-1}	Weaver et al. (1999)
$CO_2 + hv$	O I (^1D)	1.9×10^{-6} s^{-1}	Bhardwaj & Raghuram (2012)
$CO + hv$	any	3.3×10^{-6} s^{-1}	Huebner et al. (1992)
$CO + hv$	O I (^1D)	9.1×10^{-8} s^{-1}	Bhardwaj & Raghuram (2012)
$O_2 + hv$	any	4.5×10^{-6} s^{-1}	Huebner et al. (1992)
$O_2 + hv$	O I (^1D)	4.0×10^{-6} s^{-1}	Huebner et al. (1992)
$NH_3 + hv$	any	2.04×10^{-4}	Fink (2009)
$HCN + hv$	any	1.5×10^{-5} s^{-1}	Huebner et al. (1992)
$HCN + hv$	CN	1.5×10^{-5} s^{-1}	Huebner et al. (1992)
$HCN + hv$	CN ($B^2\Sigma^+$)	1.5×10^{-6} s^{-1}	Bockelée-Morvan & Crovisier (1985)
$H_2O + e-$	OH ($A^2\Sigma^+$)	8.5×10^{-22} m^2	Avakyan et al. (1998)
$H_2O + e-$	O I ($^1S + {}^1D$)	9.7×10^{-16} m^3 s^{-1}	Bhardwaj & Raghuram (2012)
$CO_2 + e-$	O I ($^1S + {}^1D$)	5.3×10^{-14} m^3 s^{-1}	Bhardwaj & Raghuram (2012)
$CO + e-$	O I ($^1S + {}^1D$)	2.9×10^{-16} m^3 s^{-1}	Bhardwaj & Raghuram (2012)
$O_2 + e-$	O I ($^1S + {}^1D$)	1×10^{14} m^3 s^{-1}	Estimated from Avakyan et al. (1998)
$O_2 + e-$	X^{q+}	1.5×10^{-20} m^2	Straub et al. (1996)
$NH_3 + e-$	NH ($A^3\Pi_1$)	2.8×10^{-22} m^2	Müller & Schulz (1992)
O I $^1D + H_2O$	2OH	2×10^{-16} m^3 s^{-1} molecule^{-1}	Streit et al. (1976)
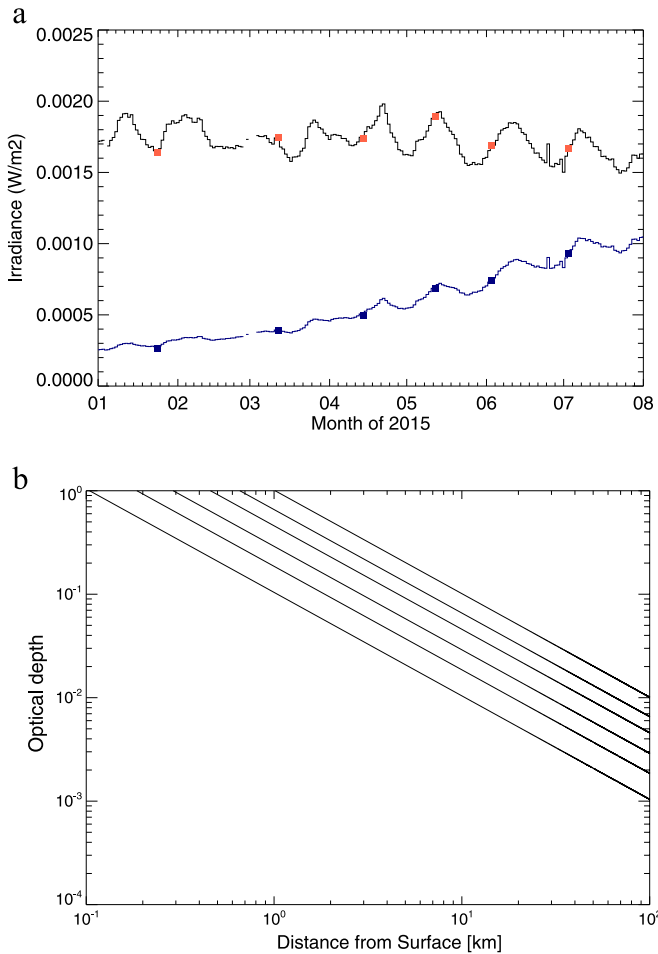
Figure 6. (a) *SDO*/EVE integrated irradiances between 30 and 100 nm at 1 au (black line) and at the heliocentric distance of 67P (blue line). Red and blue dots indicate the times of observations discussed in this paper. (b) Optical depth for light with a wavelength of 30 nm, calculated for the different observing dates, 2015 January–July from bottom to top.

Along with the gas production rates, dust production rates also increased significantly over the course of our observations. Based on *Cassini* observations, it has been suggested that nanograin charging could result in significant electron depletion (Nilsson et al. 2015b; Vigren et al. 2015). Reaction rates for attachment of electrons to grains are very low for suprathermal electrons and would mostly affect electrons with much lower energies than those responsible for the electron impact dissociation (>10 eV). We do not expect electron–dust interactions to affect the observed emission.

The most likely explanation of the decrease in emission from the inner coma is a significant decrease in the electron temperature, which reduces reaction rates. At energies of a few eV, when temperatures fall below the appearance thresholds of the dissociative reactions, the excitation of H_2O molecules becomes an effective cooling process (Cravens & Korosmezey 1986). Electrons gain energy by photoionization processes and interactions between the comet and solar wind (Clark et al. 2015), and lose energy through collisional processes, for example (Wegmann et al. 1999):

$$
\begin{aligned}
H_2O + hv &\rightarrow H_2O^+ + e \ [+12.3 \text{ eV}] \\
H_2O + e &\rightarrow H_2 + O(^1D) + e \ [-12.3 \text{ eV}] \\
H_2O + e &\rightarrow OH + H + e \ [-5.1 \text{ eV}],
\end{aligned}
\tag{5}
$$

The *Giotto* probe observed maximum ion density 12,000 km from the nucleus of 1P/Halley (Häberli et al. 1995). This was attributed to a steep increase in the electron temperature with distance to the nucleus, in turn caused by decreased cooling through collisions between electrons and neutrals.

In the period 2015 January–July, the neutral gas density increased much faster ($\sim r_h^{-4.2}$) than the increase in solar radiation ($\sim r_h^{-2}$), which should lead to a decrease in the electron temperature. The electron impact dissociation processes that produce the emission observed with OSIRIS all have relatively high appearance energies (Avakyan et al. 1998).

Cooling of the electrons below those energies could lead to an abrupt decrease in the emission.

Lastly, the observed decrease in the emission might be related to changes in the interaction between comet and solar wind. Electrons in the solar wind have higher temperatures than photoelectrons, and its interaction with the coma may heat electrons (Häberli et al. 1996; Clark et al. 2015; Broiles et al. 2016). Initially, the solar wind could penetrate deep into the coma (Nilsson et al. 2015a, 2015b). With increasing production rate, plasma boundaries separated the solar wind from the cometary gas (Rubin et al. 2015). By the end of 2015 February, the RPC/Ion Composition Analyzer measured that the proton energy spectrum started to change, indicative of an increasing interaction between comet and solar wind.

7. SUMMARY AND CONCLUSION

This study uses data from *Rosetta*'s OSIRIS camera system and presents observations of the inner coma of 67P/Churyumov–Gerasimenko acquired with narrow-band filters centered on the emission features of OH, O I, CN, NH, and NH_2. The observations explore a new regime in cometary science: the inner coma of a low-activity comet at large heliocentric distances, and the *Rosetta* mission allows us to study how this environment changed over time. We developed an extensive image reduction procedure and applied this to observations acquired between 2015 January and July, when the comet's distance to the Sun decreased from 2.5 to 1.3 au.

The observations in all filters at all epochs indicated surface brightnesses that are one or more orders of magnitude higher than can be explained by photodissociation. Instead, the emission is likely the result of dissociative electron impact excitation and/or different species. The OH emission can be attributed to electron dissociative excitation of H_2O, and the observed intensities are generally consistent with neutral column densities and electron densities observed by other instruments on board *Rosetta*. We attribute most of the [O I] 630 nm emission in the inner coma to electron impact dissociative excitation of CO_2, which has a much larger cross section than H_2O. The emission detected in the NH filter is likely the result of electron dissociative excitation that produces OH^+ ions from H_2O molecules directly in an excited state. The surface brightness levels observed in the CN filter and the similarity between the morphologies observed in the CN and [O I] filters suggest that the emission is the product both of CO_2^+ ions produced by electron impact dissociative excitation and of fluorescent emission by CN radicals. Follow-up studies of the correlation between the emission seen in CN versus [O I], and OH versus NH might provide very interesting windows on the different reaction channels from impact on the same species.

The intensity of the emission in the inner coma decreased between March and June, despite increasing gas production rates as the comet approached the Sun. The most likely explanation is that, because the gas production rates increased much faster than the ionizing solar radiation, collisions between electrons and neutral water molecules lowered electron temperatures in the inner coma below the activation threshold of the dissociative impact excitation reactions. The increase in optical depth and deflection of the solar wind may have further contributed to the electron cooling.

Our results thus show that the narrow-band filters on *Rosetta*/OSIRIS can be used to remotely study the interaction between electrons and the neutral gas in the inner coma. However, the lack of experimental cross sections hampers the interpretation of our results; the cross sections needed most urgently are those for the production of O I ^{1}D from CO_2 and H_2O, and of CN from HCN. In addition, we have identified the need for models that combine the physical and chemical processes of cometary gases with plasma characteristics such as electron temperatures.

Impact excitation may matter in different planetary environments through different interaction mechanisms (photoelectrons, solar wind protons and/or electrons). First, since the resulting emission traces the distribution of a parent species, electron impact dissociation could explain the excitation of fragments whenever a steep, radial gradient is seen in the emission morphology of the fragment species, such as in the large-scale jet-like structures around comets (A'Hearn et al. 1986). Second, under conditions similar to those of 67P, dissociative electron impact excitation can lead to significant emission by fragment species. This might lead to detectable emission from Main Belt Comets or even Ceres—or to an overestimate of production rates if only photo-processes are assumed to drive the emission of fragment species.

Comet 67P reached its perihelion on 2015 August 13, at a heliocentric distance of 1.24 au. The *Rosetta* spacecraft will continue to orbit its nucleus and study how its coma evolves while the comet moves away from the Sun again.

APPENDIX A
EMISSION MODEL

To aid in our interpretation of our results, we have developed a basic coma model, summarized below. A true model would combine a realistic distribution of the neutral gas, the cometary and solar wind plasma, and all relevant chemical and physical reactions. The complexity of such a model is outside the scope of this paper.

A.1. Neutral Density Model

Total water production rates of 67P were estimated using the empirical relation derived between water production $Q(H_2O)$ and heliocentric distance r_h by Fougere et al. (2016):

$$Q(H_2O) \sim 1.02 \times 10^{28} r_h^{-4.2} \text{ (molecules s}^{-1}). \quad (7)$$

We assumed constant abundances of $CO_2/H_2O = 3\%$, $CO/H_2O = 3\%$, $O_2/H_2O = 3.8\%$, and $HCN/H_2O = 0.1\%$ (Bieler et al. 2015b; Le Roy et al. 2015; Fougere et al. 2016). For the distribution of fragment species we assumed a standard Haser model (Festou 1981; Combi et al. 2004). The photodissociation rates of the different gases are listed in Table 7, and those were scaled with the heliocentric distance as $1/r_h^2$. We assumed that all gases are accelerated to a bulk velocity v_g within a distance $d = 200$ km from the center of the nucleus (Combi et al. 2004) using the empirical relation

$$v_g = 0.85 r_h^{-1/2} \left[1 - \exp\left(\frac{-d}{50 \text{ km}}\right) \right] \text{(km s}^{-1}). \quad (8)$$

We assumed the same bulk outflow gas velocity for both parent and fragment species.

A.2. Electrons

The electron density in the coma was measured by the Langmuir Probe (LAP) and Mutual Impedance Probe (MIP) on *Rosetta* between 2015 February 4 and 28 (2.3 au from the Sun; Edberg et al. 2015). For the electron density we assumed that the number density and radial distribution measured by LAP/MIP scaled linearly with the water production rate and the photoionization rate (and thus the square of the heliocentric distance):

$$n_e = \frac{Q_{H_2O}}{10^{26}} \times \frac{10^{14}}{d} \times \frac{3}{r_h^2} \text{ (m}^{-3}), \quad (9)$$

where n_e denotes the electron density and d the distance from the comet's surface. Rather than assuming a temperature distribution, we assumed a fixed electron temperature of 30 eV (3.3×10^6 m s^{-1}) for electron fluxes and for the cross sections of electron impact reactions. To calculate the emission resulting from dissociative electron impact dissociation, we multiplied the neutral density in the coma $n(d)$ at a distance d from the nucleus by the local electron density $n_e(d)$, electron velocity v_e, and emission cross section σ or by the reaction rate where applicable (Table 7):

$$S(d) = \frac{n(d) n_e(d) v_e \sigma}{4\pi} \text{ (photons s}^{-1} \text{ m}^{-3}). \quad (10)$$

This is then integrated over the line of sight (from the position of the spacecraft Δ to infinity) to produce the surface brightnesses $B(\theta)$ as a function of the angle between the spacecraft–comet line and the comet–Sun line:

$$B(\theta) = \int_{\Delta}^{\infty} \frac{S(d)}{4\pi} \delta d \text{ (photons s}^{-1} \text{ m}^{-2} \text{ sr}^{-1}). \quad (11)$$

The radial distance d from the nucleus in any position in the comet–Sun–spacecraft plane can be calculated using the cosine rule.

A.3. O I Quenching and Transport

The [O I] 630 nm emission is different from the other emission features because it is a forbidden line, and we expect quenching of the O I ^1D state by the reaction O I ^1D + $H_2O \rightarrow 2OH$ to decrease the [O I] 630 nm emission with increasing production rates. The O I ^1D state has a long lifetime of 101 s (Atkinson et al. 1997). To assess the effect of the deactivation of O I ^1D through collisions with H_2O on the surface brightness profile we combined the Haser model from Appendix A.1 and adopted experimental rate coefficients of 2×10^{-19} m^3 s^{-1} molecule^{-1} (Streit et al. 1976). To correct for excited O I atoms lost through collisional quenching, we calculate an effective density $n'(d)$ by weighting the neutral gas density function $n(d)$ from Equation (9) by a correction factor. Assuming a quenching rate R (Table 7), the distance $l(d)$ that an O I atom moving with velocity v_d can travel before colliding is

$$l(d) = \frac{v_d}{Rn(d)}. \quad (12)$$

Now the fraction of atoms that can emit and thus are not quenched is given by

$$n'(d) = n(d) \left[1 - \exp\left(\frac{-l(d)}{v_d \tau}\right) \right], \quad (13)$$

where τ is the lifetime of the O I ^1D state (101 s), and $n(d)$ the density of neutral water at a distance d from the surface. We assumed a fixed distance between comet and spacecraft of 100 km to evaluate the effect of quenching and have added the [O I] emission from all H_2O and CO_2 processes (the dominant contributions to the O I emission, see Figure 5 in the main text). In January, only the first kilometer is affected by quenching in the inner coma. In July, the innermost 3 km are affected, and at 1 km approximately the observed surface brightness is approximately 50% of the emitted light.

In addition, because of the long lifetime of the ^1D state, only some of the atoms decay to the ground state within the field of view. We account for this with a second correction factor:

$$n''(d) = n'(d) \left[1 - \exp\left(\frac{-d}{v_d \tau}\right) \right]. \quad (14)$$

The results, again for a fixed spacecraft distance of 100 km, are shown in Figures 5(c) and (d). The effect of the O I ^1D lifetime is dramatic: it flattens the surface emission in the first few kilometers around the nucleus.

A.4. Optical Depth

With increasing gas production rates, the optical depth of the inner coma increases and fewer photoelectrons are produced. To investigate the optical depth of the coma, we calculated H_2O column densities using a Haser distribution (Section 3.3), and assumed water production rates from the empirical formula by Fougere et al. (2016, see also Figure 4(a)). The dominant photons for ionization have wavelengths between 30 and 85 nm (Huebner et al. 1992; Budzien et al. 1994). At these two wavelengths, H_2O has photoabsorption cross sections of 1.0×10^{-21} m^2 and 1.6×10^{-21} m^2, respectively (Phillips et al. 1977). The results are shown in Figure 6(b). The relevant region here is between 1 and 10 km from the surface. In January, only 1%–10% of photons were lost within this region. The effect of the increasing optical depth on the neutrals and

electrons in the inner coma is not included in the surface brightness model.

REFERENCES

A'Hearn, M. F., Belton, M. J. S., Delamere, W. A., et al. 2005, Sci, 310, 258
A'Hearn, M. F., Belton, M. J. S., Delamere, W. A., et al. 2011, Sci, 332, 1396
A'Hearn, M. F., Hoban, S., Birch, P. V., et al. 1986, Natur, 324, 649
A'Hearn, M. F., Krishna Swamy, K. S., Wellnitz, D. D., & Meier, R. 2015, AJ, 150, 5
Ajello, J. M. 1971, JCP, 55, 7
Atkinson, R., Baulch, D. L., Cox, R. A., et al. 1997, JPCRD, 26, 1329
Avakyan, S. V., Il'in, R. N., Lavrov, V. M., & Ogurtsov, G. N. 1998, in Collision Processes and Excitation of UV Emission from Planetary Atmospheric Gases: A Handbook of Cross Sections, ed. S. V. Avakyan (Amsterdam: Gordon and Breach)
Bhardwaj, A., & Raghuram, S. 2012, ApJ, 748, 13
Bieler, A., Altwegg, K., Balsiger, H., et al. 2015a, A&A, 583, A7
Bieler, A., Altwegg, K., Balsiger, H., et al. 2015b, Natur, 526, 678
Bockelée-Morvan, D., & Crovisier, J. 1985, A&A, 151, 90
Bockelée-Morvan, D., Debout, V., Erard, S., et al. 2015, A&A, 583, A6
Broiles, T., Livadiotis, G., Burch, J. L., et al. 2016, J. Geophys. Res., 121, 7407
Brownlee, D. E., Horz, F., Newburn, R. L., et al. 2004, Sci, 304, 1764
Budzien, S. A., Festou, M. C., & Feldman, P. D. 1994, Icar, 107, 164
Clark, G., Broiles, T. W., Burch, J. L., et al. 2015, A&A, 583, A24
Cochran, A. L. 2002, Icar, 157, 297
Cochran, A. L. 2008, Icar, 198, 181
Combi, M. R., Harris, W. M., & Smyth, W. H. 2004, in Comets II, ed. M. C. Festou, H. U. Keller, & H. A. Weaver (Tucson, AZ: Univ. Arizona Press), 523
Cravens, T. E., & Korosmezey, A. 1986, PSS, 34, 961
Edberg, N. J. T., Eriksson, A. I., Odelstad, E., et al. 2015, GeoRL, 42, 4263
Farnham, T. L., Schleicher, D. G., & A'Hearn, M. F. 2000, Icar, 147, 180
Feldman, P. D., A'Hearn, M. F., Bertaux, J.-L., et al. 2015, A&A, 583, A8
Festou, M. C. 1981, A&A, 95, 69
Fink, U. 2009, Icar, 201, 311
Fougere, N., Altwegg, K., Berthelier, J.-J., et al. 2016, A&A, 588, A134

Fray, N., Benilan, Y., Cottin, H., Gazeau, M.-C., & Crovisier, J. 2005, PSS, 53, 1243
Gulkis, S., Allen, M., Von Allmen, P., et al. 2015, Sci, 347, 0709
Häberli, R., Altwegg, K., Balsiger, H., & Geiss, J. 1996, JGR, 101, 15579
Häberli, R. M., Altwegg, K., Balsiger, H., & Geiss, J. 1995, A&A, 297, 881
Huebner, W. F., Keady, J. J., & Lyon, S. P. 1992, Ap&SS, 195, 1
Kawakita, H., & Watanabe, J.-I. 2002, ApJ, 572, L177
Keller, H. U., Delamere, W. A., Huebner, W. F., et al. 1987, A&A, 187, 807
Keller, H. U., Kueppers, M., Fornasier, S., et al. 2007, SSRv, 128, 433
Keller, H. U., Mottola, S., Skorov, Y., & Jorda, L. 2015, A&A, 579, L5
Kim, S. J., A'Hearn, M. F., & Cochran, W. D. 1989, Icar, 77, 98
Le Roy, Altwegg, K., Balsiger, H., et al. 2015, A&A, 583, A1
Magrin, S., La Forgia, F., Da Deppo, V., et al. 2015, A&A, 574, A123
McConkey, J. W., Malone, C. P., Johnson, P. V., et al. 2008, PhR, 466, 1
Müller, U., Bubel, T., & Schulz, G. 1992, ZPhyD, 25, 167
Müller, U., & Schulz, G. 1992, JChPh, 96, 5924
Nilsson, H., Stenberg Wieser, G., Behar, E., et al. 2015a, Sci, 347, 0571
Nilsson, H., Stenberg Wieser, G., Behar, E., et al. 2015b, A&A, 583, A20
Nishiyama, I., Kondow, T., & Kuchitsu, K. 1979, CPL, 62, 462
Phillips, E., Lee, L. C., & Judge, D. L. 1977, Journal of Quantitative Spectroscopy, 18, 309
Rubin, M., Gombosi, T. I., Hansen, K. C., et al. 2015, EMP, 116, 141
Schleicher, D. G. 2010, AJ, 140, 973
Schleicher, D. G., & A'Hearn, M. F. 1988, ApJ, 331, 1058
Snodgrass, C., Jehin, E., Manfoid, J., et al. 2016, A&A, 588, A80
Soderblom, L. A., Becker, T. L., Bennett, G., et al. 2002, Sci, 296, 1087
Straub, H. C., Lindsay, B. G., Smith, K. A., & Stebbings, R. F. 1996, JCP, 105, 4015
Streit, G. E., Howard, C. J., Schmeltekopf, A. L., Davidson, J. A., & Schiff, H. I. 1976, JChPh, 65, 4761
Tubiana, C., Böhnhardt, H., & Agarwal, J. 2011, A&A, 527, A113
Tubiana, C., Guettler, C., Kovacs, G., et al. 2015, A&A, 583, A46
Veverka, J., Klaasen, K., A'Hearn, M., et al. 2013, Icar, 222, 424
Vigren, E., Galand, M., Lavvas, P., & Eriksson, A. I. 2015, ApJ, 798, 130
Weaver, H. A., Feldman, H. A., A'Hear, M. F., et al. 1999, Icar, 141, 1
Wegmann, R., Jockers, K., & Bonev, T. 1999, PSS, 47, 745
Woods, T. N., Eparvier, F. G., Hock, R., et al. 2012, SoPh, 275, 115